ESA Contract Report

SMOS ESL contract 4000130567/20/I-BG

Contract Report to the European Space Agency

Annual SMOS brightness temperature monitoring report - 2024/25

Authors: Jana Kolassa, Pete Weston, Kirsti Salonen and Patricia de Rosnay
Contract officer: Raffaele Crapolicchio

November 2025

Series: ECMWF - ESA Contract Report

A full list of ECMWF Publications can be found on our web site under:

http://www.ecmwf.int/publications/

European Centre for Medium Range Weather Forecasts, Shinfield Park, Reading, RG2 9AX, UK

Abbreviations

BUFR ..... Binary Universal Form for the Representation of meteorological data
CMEM ..... Community Microwave Emissivity Modelling platform
ECMWF ..... European Centre for Medium-range Weather Forecasts
ESA ..... European Space Agency
IFS ..... Integrated Forecast System
NRT ..... Near Real Time
NWP ..... Numerical Weather Prediction
RFI ..... Radio Frequency Interference
SMAP ..... Soil Moisture Active Passive
SMOS ..... Soil Moisture and Ocean Salinity
Tb ..... Brightness Temperature

1. Introduction

This document provides an annual summary of the performance of the European Space Agency (ESA) Soil Moisture and Ocean Salinity (SMOS) brightness temperature (Tb) monitoring run routinely at the European Centre for Medium-range Weather Forecasts (ECMWF). The period covered is September 2024 to August 2025. Several different monitoring plots are presented, and notable features are discussed in detail. Also, potential improvements to the monitoring system are proposed.

2. Annual SMOS monitoring results

Routine operational monitoring of SMOS observations from the near real time BUFR (Binary Universal Form for the Representation of meteorological data) product is performed at ECMWF. The SMOS measured brightness temperatures are compared to short-term numerical weather prediction (NWP) forecasts transformed into brightness temperatures using the Community Microwave Emissivity Model (CMEM; de Rosnay et al. 2020). The CMEM outputs are simulated brightness temperatures in the Earth frame, and these are converted into the SMOS antenna frame using the geometric and Faraday rotation angles provided with each observation in the BUFR files. Differences between observations and their model counterparts are known as first-guess departures and statistics of these first-guess departures are accumulated and plotted routinely.

The samples used to produce the plots can be filtered by area, including global, Northern and Southern Hemispheres, as well as loose definitions of the continents: Europe (120°W-120°E, 35°N-77.5°N), Asia (0°W-120°W, 40°N-82.5°N), North America (120°E-0°E, 20°N-77.5°N), South America (120°E-0°E, 40°S-17.5°N) and Australia (0°E-120°W, 47.5°S-7.5°S). This Section focuses on global statistics.

The plots are produced separately for data:

- Over sea or over land
- With different incidence angles: 30°, 40° or 50°
- With different polarisations: H (XX) or V (YY) at the SMOS antenna reference frame
- RFI unscreened/screened
- Ascending and descending orbits

A selection of different options for surface type, incidence angles and polarisations is presented, and the full set of plots for the RFI screened data are available via FTP at ftp://bolftp.ecmwf.int/Annual_report_plots/All_plots_2024_2025.zip

A thorough introduction to the monitoring system can be found in Salonen et al. (2024b) and examples of the plots produced can be seen at https://www.ecmwf.int/en/forecasts/quality-our-forecasts/monitoring/smos-monitoring, where additional monitoring statistics for data without RFI screening are available as well. In this report the focus is on RFI screened data.

The following of this Section presents the different types of plots produced as part of the SMOS monitoring system, Section 3 highlights and investigates any notable features in more detail, Section 4 investigates the potential impact from the Arm-A1 temperature increase, and Section 5 presents a comparison with the equivalent monitoring statistics computed for the Soil Moisture Active Passive (SMAP) mission.

2.1. Time series

In the time series figures, statistics are plotted as lines against time on the x-axis for the full twelve-month period with statistics accumulated in 12-hour chunks. The statistics plotted are mean and standard deviation of the first-guess (FG) departures, the mean observed and first-guess brightness temperatures (Tbs) and number of observations (OBS). These plots allow global trends and jumps in the statistics to be identified.

Figures 1 and 2 show the first-guess departure statistics over land for an incidence angle of 40° for H and V polarisation, respectively. These figures indicate that the first-guess departures over land remain generally stable throughout the performance period. The mean first-guess departures mostly remain within ±7K for H polarisation Tbs and ±3K for V polarisation Tbs, respectively. The corresponding mean standard deviation of the first-guess departures is ~18K for the H polarisation and ~14K for the V polarisation channels. A slight seasonality is evident in the statistics, driven by seasonal variations in the number of observations, which are typically higher during the boreal summer when more of the Earth's land surface is unfrozen. Overall, the statistics are comparable to those reported for 2023/24 (Salonen et al., 2025), confirming that SMOS continues to operate in a stable manner. The slightly better performance observed for V polarisation compared to H polarisation may reflect an instrument-related effect, but it could also be linked to differences in the performance of the CMEM observation operator used to convert model soil moisture into brightness temperature. It is important to note that the first-guess departures presented here are not bias-corrected, and the statistics are consistent with those reported for the 2010–2016 period without bias correction (de Rosnay et al., 2020).

Despite the general stability of the statistics, there are some notable features. For example, there is a gap in the time series on 10th September 2024 due to a network outage that prevented several BUFR files from being delivered. The first time step following this outage shows a large first-guess departure, which quickly returns to normal levels. Additionally, there is an increased standard deviation of the first guess departure on 4th April 2025, as well as on 5th March 2025 in the H polarisation. These two features will be discussed in more detail in Sections 3.1 and 3.6 respectively.

Figure 3 shows the corresponding first-guess departure statistics over the ocean for an incidence angle of 40° and H polarisation. As for the land, the statistics over the ocean are generally stable with a slight seasonality caused by a seasonality in the number of observations related to fraction of ocean covered by sea-ice. The mean first guess departure as well as the mean standard deviation of the first guess departure generally stay around ~5K. The standard deviation of the first guess departure over the ocean shows an increased variability in September and October 2024. It also displays the same increased standard deviation of the first guess departure on 4th April that was observed over land and an additional similar feature can be observed on 20th March. These features will be discussed in detail in Section 3.

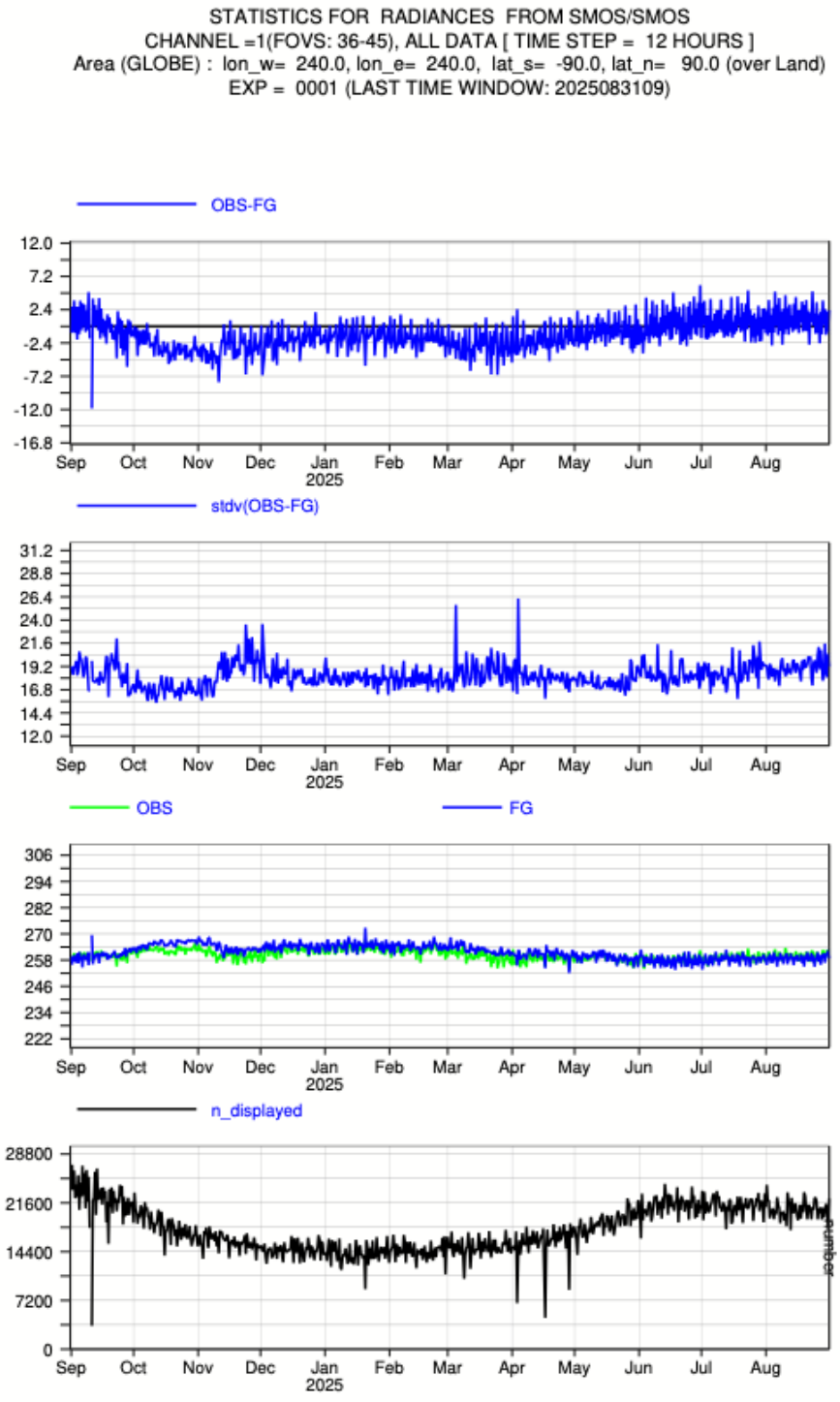

Figure 1: Time series of mean first-guess departures (upper panel), standard deviation of first-guess departures (2nd panel), mean observed and first-guess values (3rd panel) and number of observations (lower panel). Statistics are accumulated into 12-hour bins for SMOS observations over land at 40° incidence angle, H polarisation and cover 1st September 2024 to 31st August 2025.

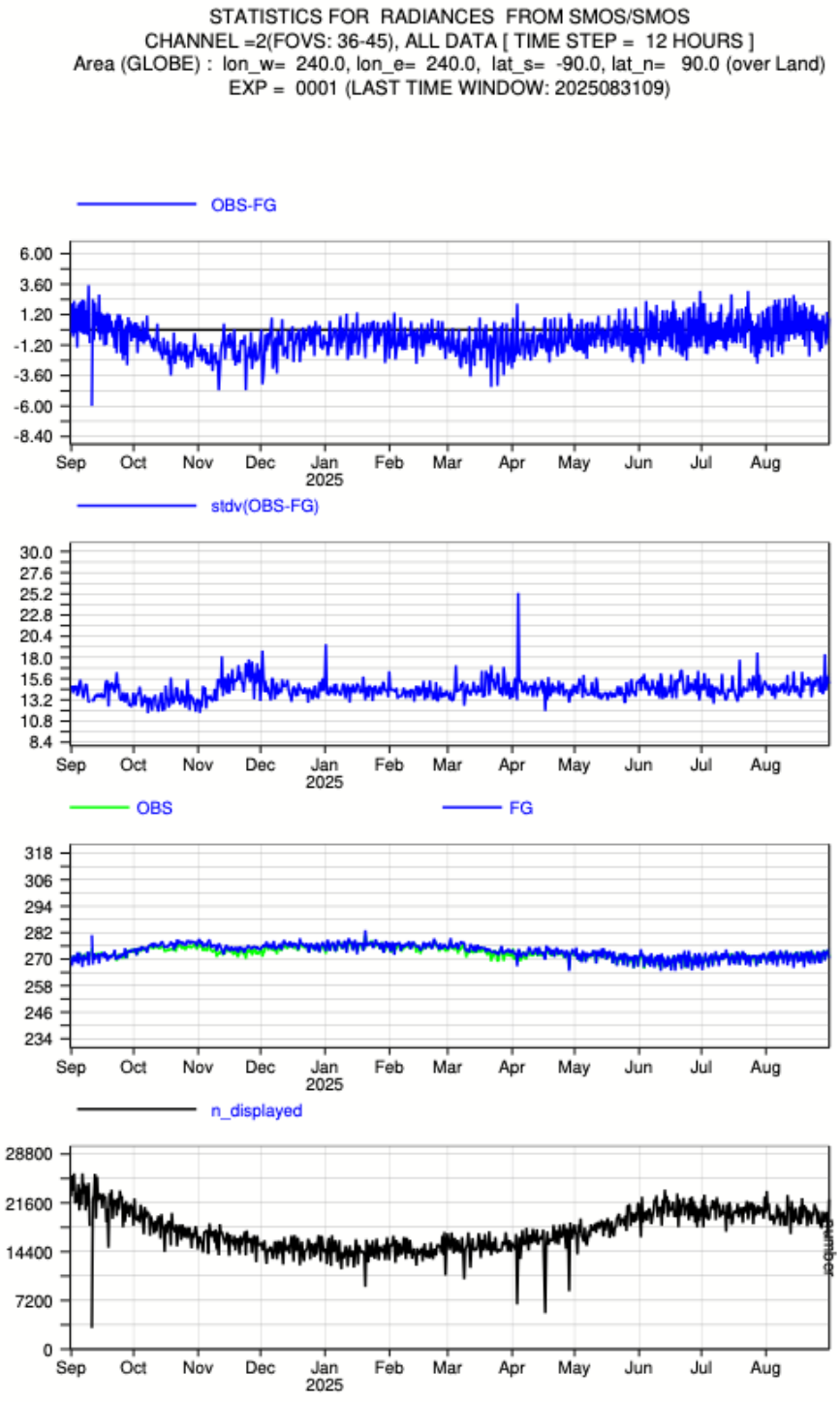

Figure 2: As figure 1 but for SMOS observations with V polarisation

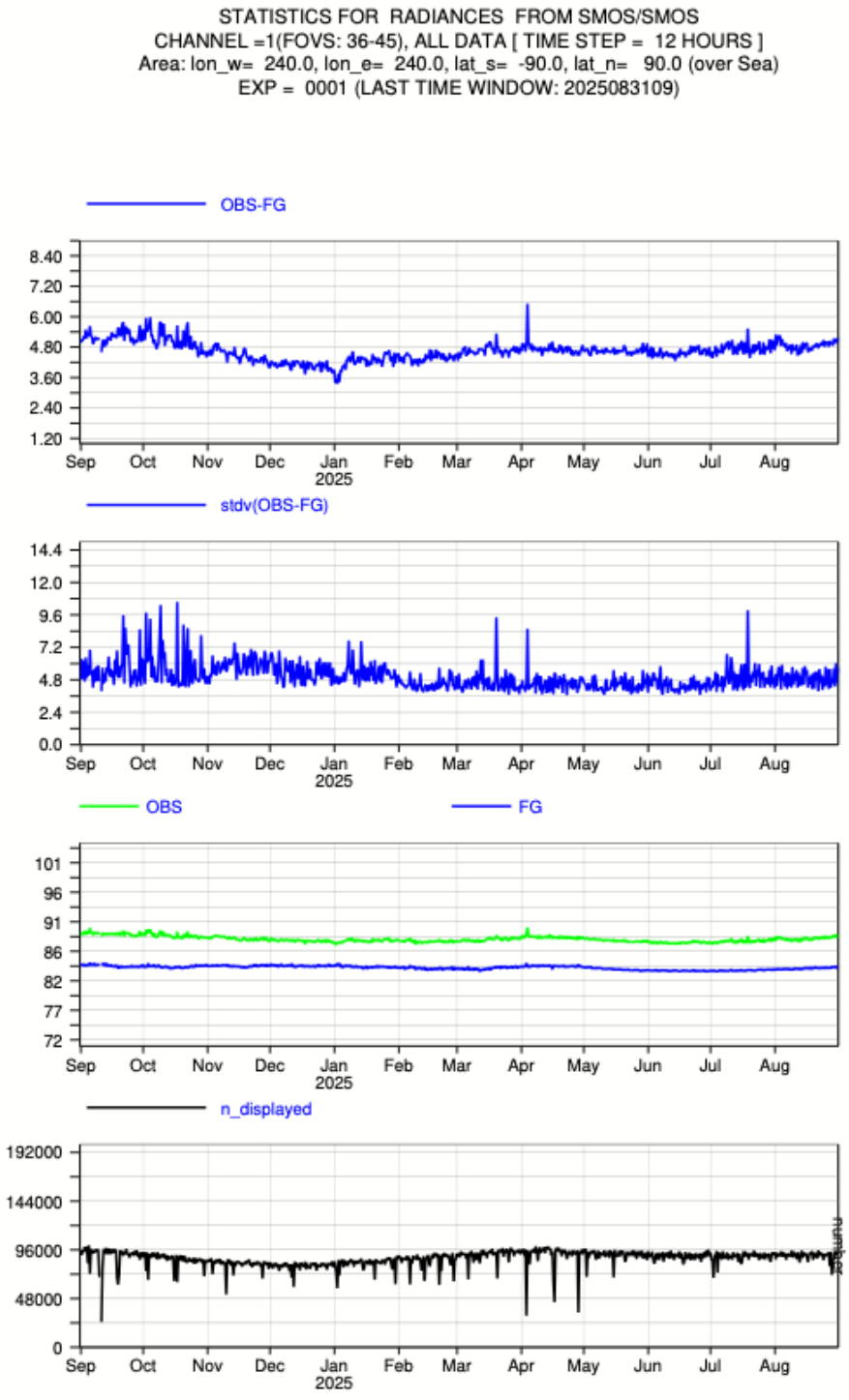

Figure 3: As figure 1 but statistics are accumulated for SMOS observations over sea at 40° incidence angle and H polarisation.

2.2. Hovmöller plots

Statistics presented in this Section are plotted as a heat map (Hovmöller plot) with time on the x-axis and latitude on the y-axis for the twelve-month period with statistics accumulated in 2.5° latitude bins and 12-hour chunks. The statistics plotted are mean and standard deviation of the first-guess departure, mean and standard deviation of the observed value, and the number of observations. These plots allow local trends and jumps in the statistics to be identified.

Figure 4 shows a Hovmöller plot of the standard deviation of the first guess departure over land for V polarisation Tbs at 30° incidence angle. A notable feature are the increased standard deviations of the first-guess departure between 60-80°N in the boreal summer that are caused by a positive bias in the first-guess departures over Siberia. Also visible are increased standard deviations of the first guess departure between 10-40°S that correspond to the wet season in Australia and South America and are likely caused by a higher variability in model precipitation leading to higher variability in model soil moisture. Finally, there is a persistent band of increased variability between 10-30°N that is caused by the combination of two effects. Throughout the year, it is caused by residual RFI near India and Southern China (see also Section 3.2), while in the boreal winter months the feature is further strengthened as a result of the wet season in that area and the associated increased variability in precipitation leading to an increased variability in soil moisture.

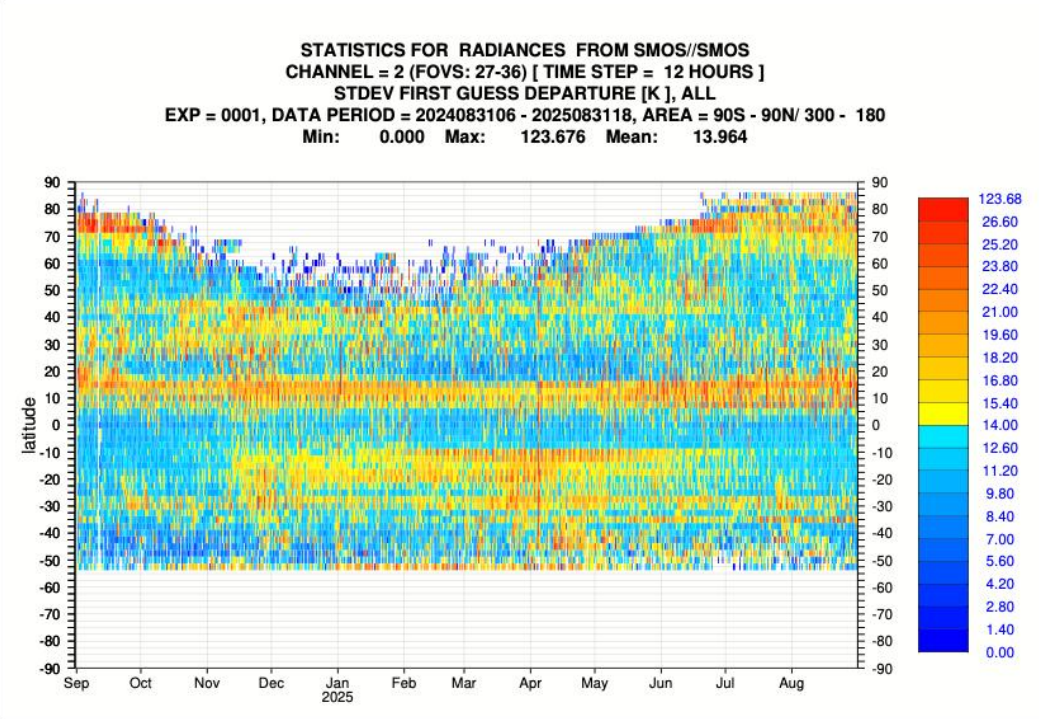

Figure 4: Hovmöller plot showing SMOS first-guess departure standard deviation monitored over land at 30° incidence angle, V polarisation covering 1st September 2024 to 31st August 2025

Figure 5 presents a Hovmöller plot of the first-guess departure standard deviation for 20° incidence angle H-polarisation data over the ocean. Overall, variability is higher in the Northern Hemisphere compared to the Southern Hemisphere, likely due to increased RFI near the coasts of Europe and Asia. A notable feature appears between 0° and 45°N from November 2024 to February 2025, associated with an increase in observation standard deviation within the same latitude band and a decrease in observation counts in the Southern Hemisphere (Figure 6). This feature, which is less prominent at higher incidence angles, has been observed in previous years and is attributed to a solar effect, which will be discussed in detail in Section 3.4. However, as discussed in Sections 3.2 and 3.3, the features appearance in the standard deviation of the observations and the first-guess departure is partly driven by residual RFI at these latitudes.

Another feature of elevated standard deviations occurs between 15° and 35°N during September and October, corresponding to increased variability seen in the time-series plots. This feature will be addressed in Section 3.3.

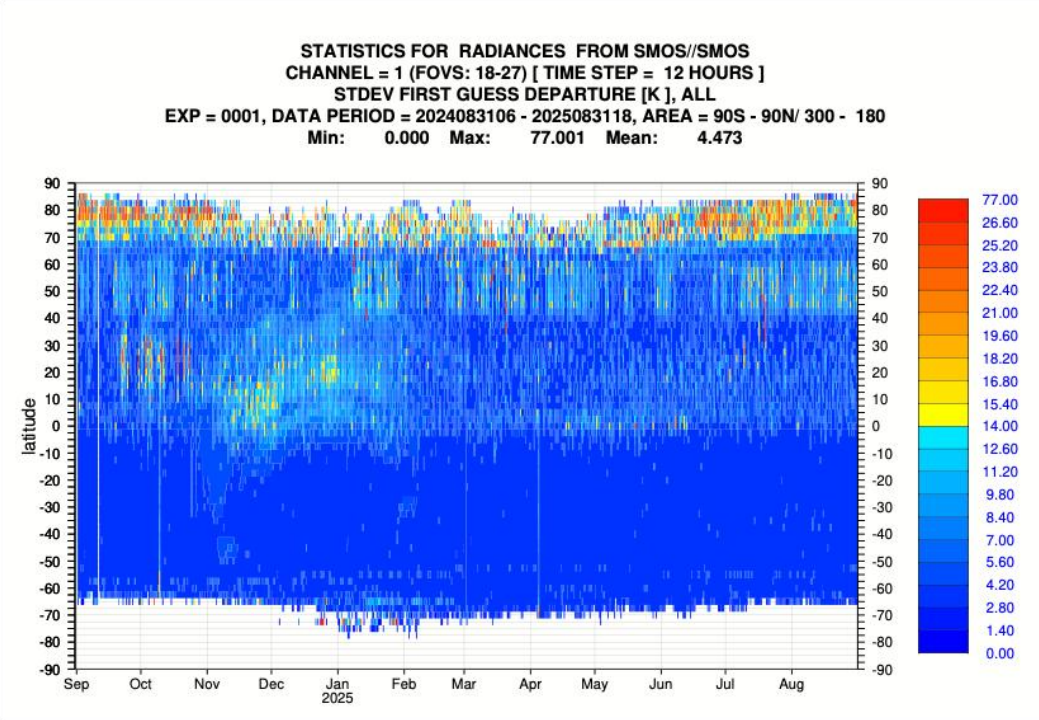

Figure 5: Hovmöller plot showing first guess departure standard deviation monitored over sea at H polarisation and 20° incidence angle. The period covered is 1st September 2024 to 31st August 2025.

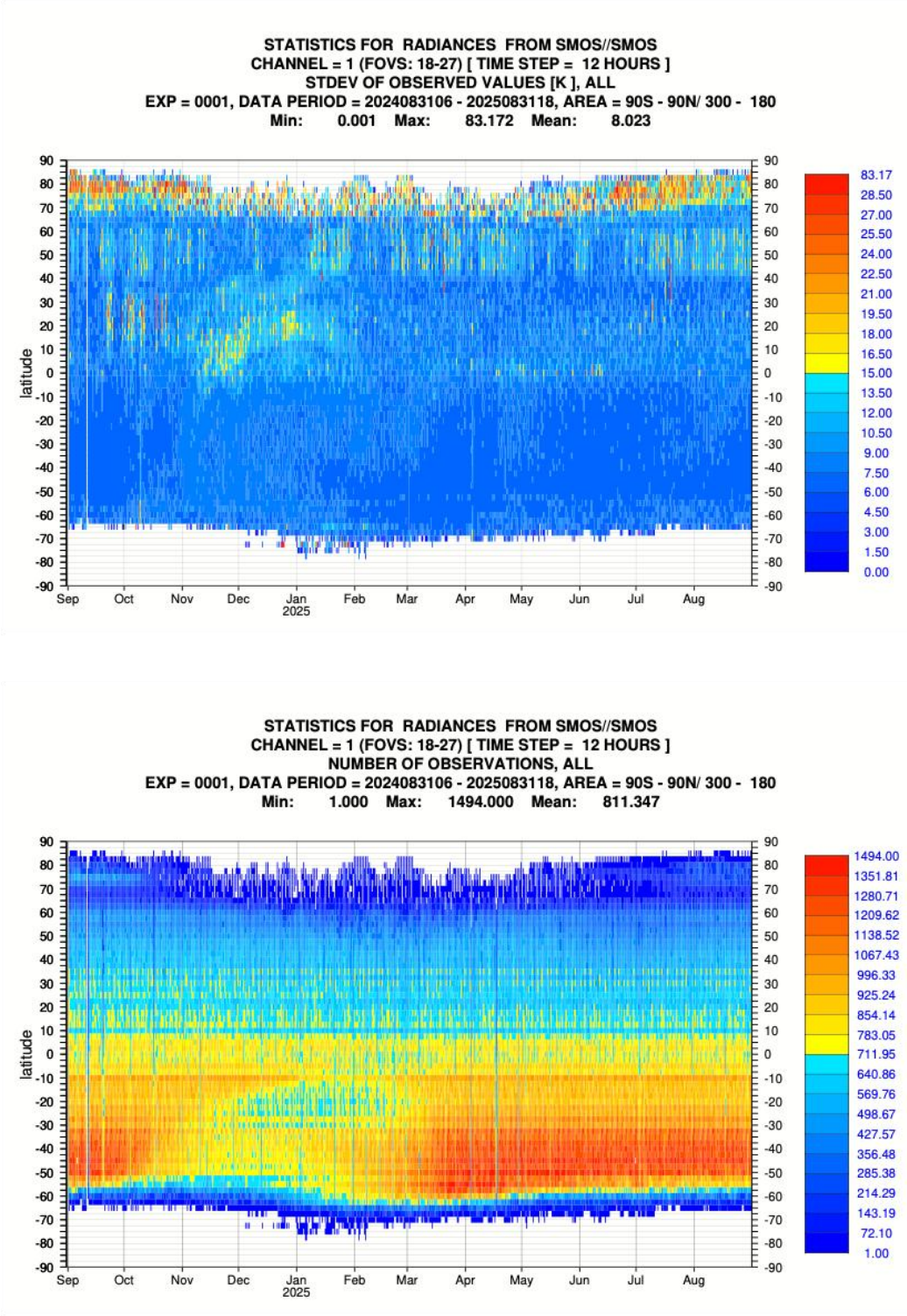

Figure 6: Hovmöller plot showing observation standard deviation (top panel) and number of observations (bottom panel) over sea at H polarisation and 20° incidence angle. The period covered is 1st September 2024 to 31st August 2025.

2.3. Maps

Figure 7 shows the geographical distribution of biases in the SMOS first-guess departures over land and Figure 8 shows the corresponding standard deviation of the first-guess departures. The standard deviation is dominated by a pronounced feature of increased variability over India and southern China, which coincides with a region of large negative mean first-guess departures in Figure 7. An inspection of the monthly maps of the first-guess standard deviation indicates that this feature occurs between November 2024 and January 2025 and is likely associated with a new RFI source, which in this case decreases the brightness temperature. Further details are provided in Section 3.2.

Figures 9 and 10 show the mean first-guess departures and their standard deviation for the performance period when excluding November 2024 to January 2025. While Figures 1 and 2 indicated relatively small global mean first-guess departures of less than 10K, Figure 9 illustrates than local biases can frequently exceed 20K. Large positive biases are observed over Europe, Northern and Eastern Asia and South America, whereas large negative biases are evident over large parts of Africa, South-Western Asia, Australia and Central and far North of North America. The spatial distribution of these biases closely resembles that reported for 2023/24 by Salonen et al. (2025).

Figure 10 indicates that the greatest variability in first-guess departures persists over the Middle East, Central and Eastern Asia, and Europe. This variability is primarily driven by RFI in these regions, with the strength and location of RFI sources varying significantly throughout the year. The RFI situation over Europe, linked to the war in Ukraine, appears to have deteriorated compared to 2023/24, with noticeably larger areas being removed through RFI filtering. Despite substantial improvements in RFI screening, Figure 10 demonstrates that the filtering remains imperfect, as large areas still exhibit residual contamination.

Figure 11 shows the first-guess departure standard deviation over the ocean for a 30° incidence angle and H-polarisation. Areas of increased variability are evident near the coasts of Europe and Asia, as well as in the Arctic Ocean. Compared to 2024/25 (Salonen et al., 2025), the variability in the first-guess departures in these regions has increased significantly, likely due to intensified RFI over Europe and new contamination sources over India and China, as indicated by the land maps. Over the Northern and Southern polar regions, the increased variability is likely driven by smaller sample sizes resulting from sea-ice screening and slight model sub-optimalities during rapid melting and freezing events. Outside RFI-affected and polar regions, variability in first-guess departures remains minimal, reflecting the relatively low brightness temperature variations over ocean, which are primarily linked to temperature changes. Additionally, the observation operator CMEM currently treats sea surfaces as flat, similar to lakes. Therefore, simulated brightness temperatures do not account for variations caused by waves or surface wind speed, unlike the observed brightness temperatures.

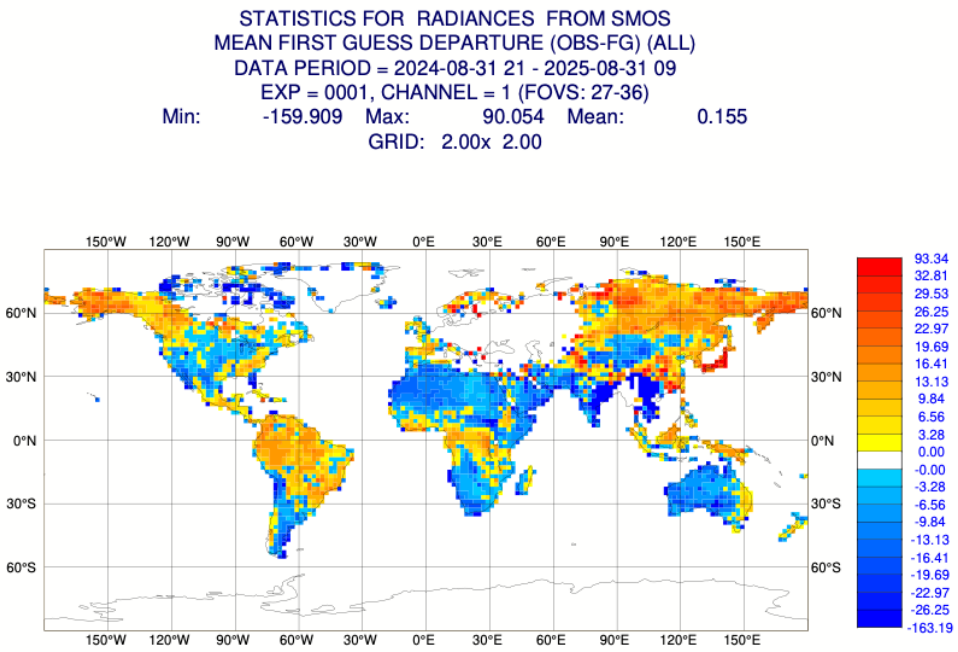

Figure 7: Gridded map plot showing the mean of SMOS first-guess departures over land at 30° incidence angle, H polarisation covering 1st September 2024 to 31st August 2025.

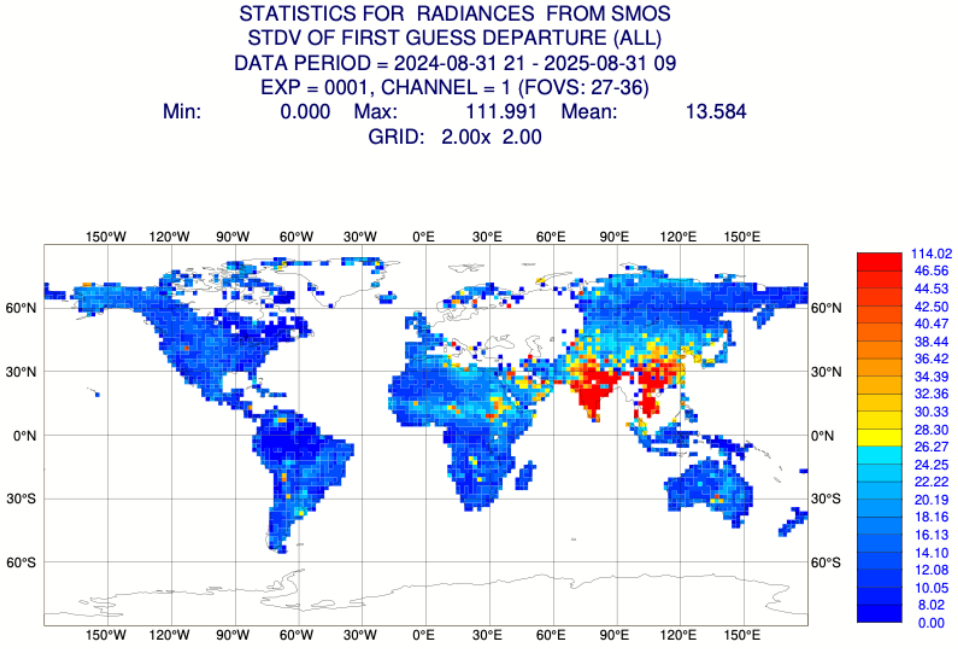

Figure 8: Gridded map plot showing the standard deviation of SMOS first-guess departures over land at 30° incidence angle, H polarisation covering 1st September 2024 to 31st August 2025.

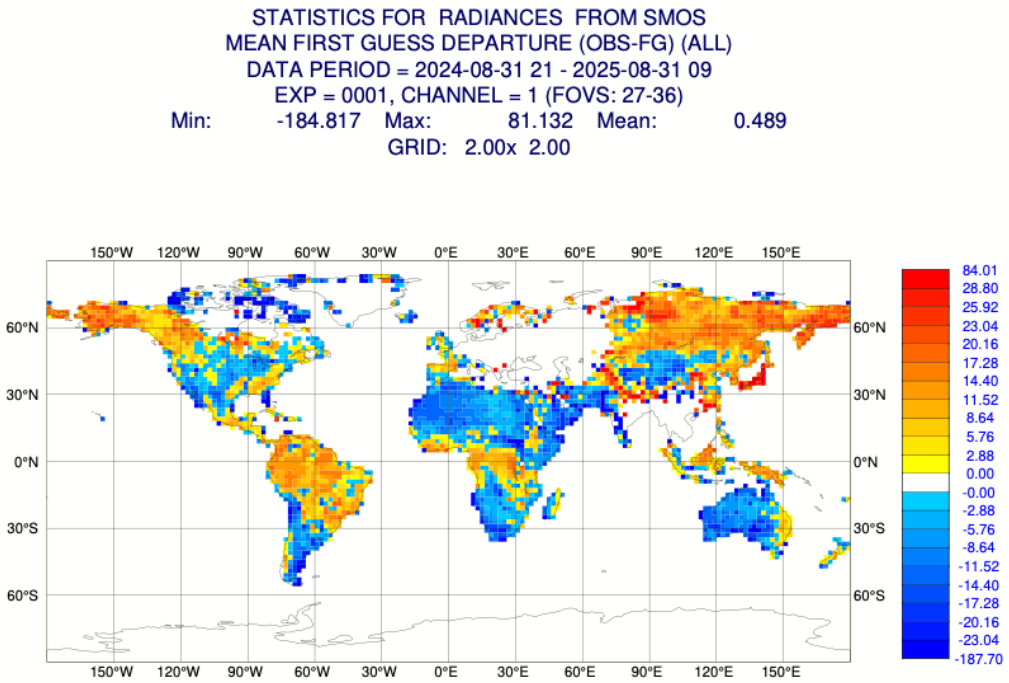

Figure 9: Same as Figure 7, but with November 2024 – January 2025 removed from the statistics computation.

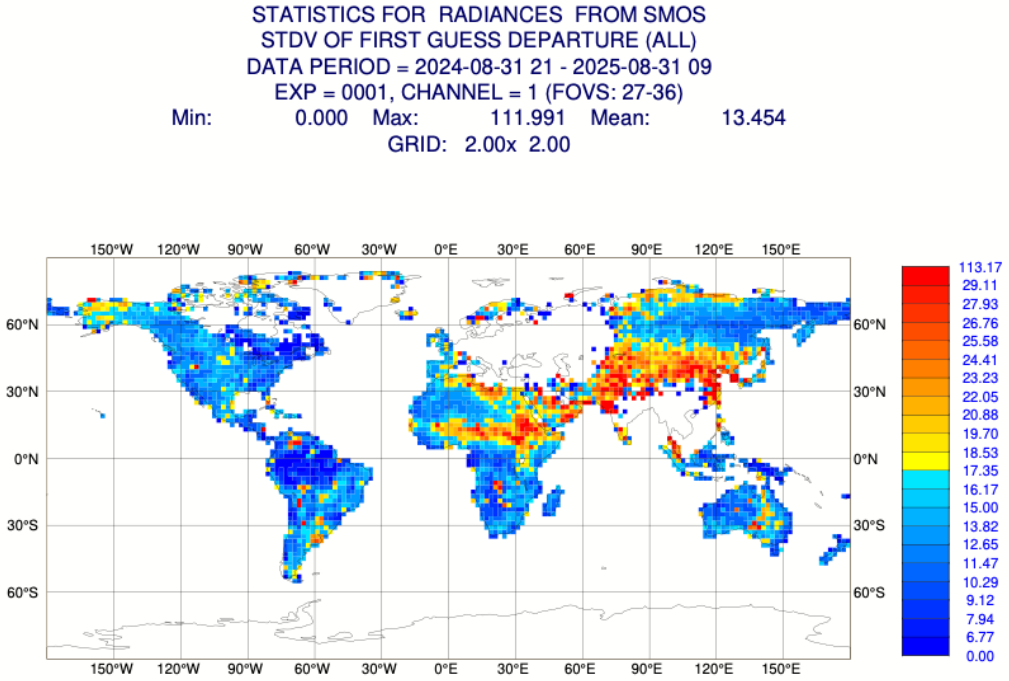

Figure 10: Same as Figure 8, but with November 2024 – January 2025 removed from the statistics computation.

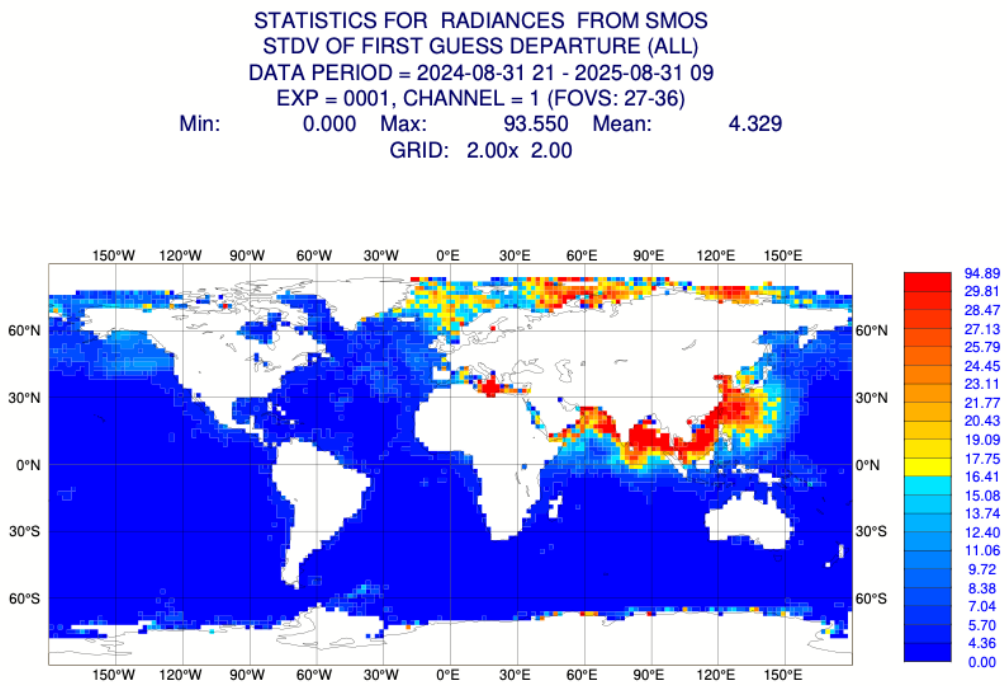

Figure 11: Gridded map plot showing the standard deviation of SMOS first-guess departures over sea at 30° incidence angle, H polarisation covering 1st September 2024 to 31st August 2025.

2.4. Scatter plots

In the scatter plots, statistics are accumulated from 1st September 2024 to 31st August 2025 and plotted as a 2-dimensional histogram with incidence angle on the x-axis and first-guess departure on the y-axis. These plots allow the distributions of first-guess departures at different incidence angles to be analysed.

Figure 12 shows that the distribution of first-guess departures is centred close to zero and symmetric for the 40° and 50° incidence angle bins. There is an apparent slight asymmetry in the 30° incidence angle bin, with the peak of the distribution slightly favouring negative first-guess departure values. This could be an effect of the patch of persistent negative first-guess departures over India and China, that was noted in Section 2.3 and that will be discussed further in Section 3.2. Compared to 2023/24 (Salonen et al., 2025), the total number of observations has decreased, which can be attributed to the more extensive RFI filtering due to increase in RFI contamination in some areas as remarked in Section 2.3. The global mean first-guess departures for each incidence angle bin are close to zero although there are significant regional biases, see Section 2.3.

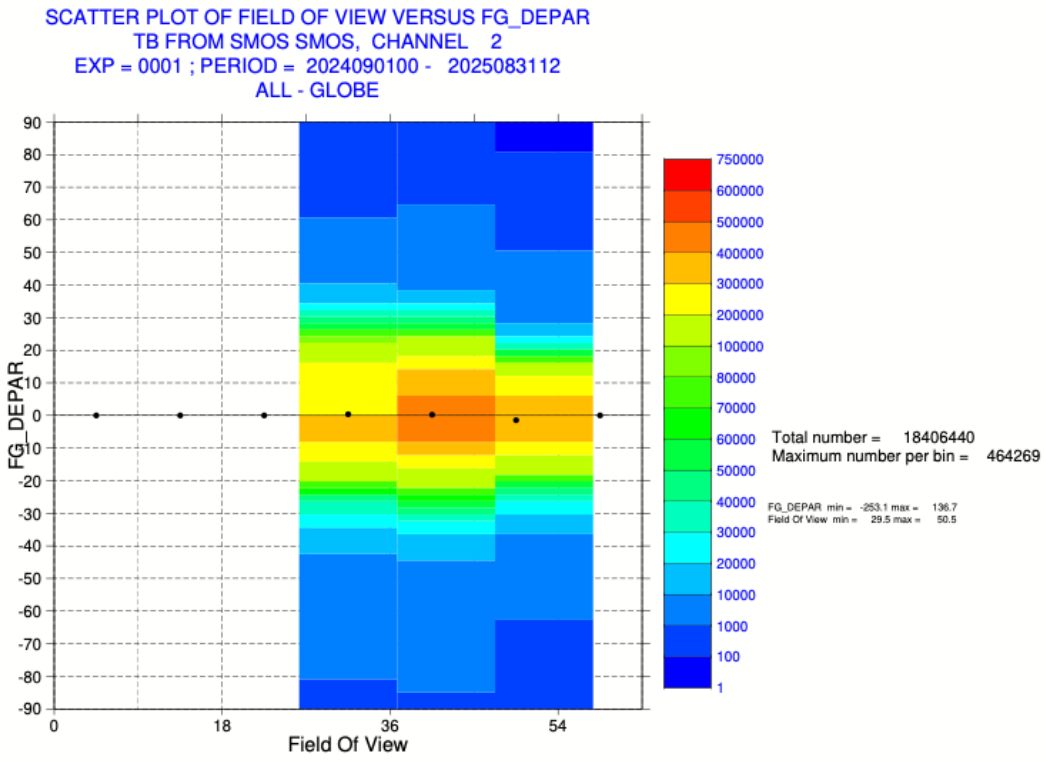

Figure 12: Scatter plot showing a 2D-histogram of SMOS first-guess departures over land for different incidence angle bins, V polarization covering 1st September 2024 to 31st August 2025. The black dots represent the mean first-guess departure for each incidence angle bin.

3. Notable features in 2024/2025

This Section describes notable features which are visible in the monitoring plots for September 2024 to August 2025.

3.1. Increased variability in first-guess departures on 4th April 2025

On 4th April 2025, the time series plots for land and ocean (Figures 1 - 3) display a high standard deviation of the first-guess departures. An examination of the Hovmöller plots for the surrounding period reveals a significant reduction in observation counts at 12UTC on 3rd April, followed by a return to normal levels in the subsequent time step (upper panel of Figures 13 and 14). However, this recovery was accompanied by a substantially higher standard deviation of the first guess departures across all latitudes for both ocean (bottom panel Figure 13) and land (bottom panel Figure 14), which is a result of increased observation standard deviations (not shown). The reduction in observation numbers was caused by delayed delivery of input BUFR files due to processor issues, as reported in Weston et al., 2025.

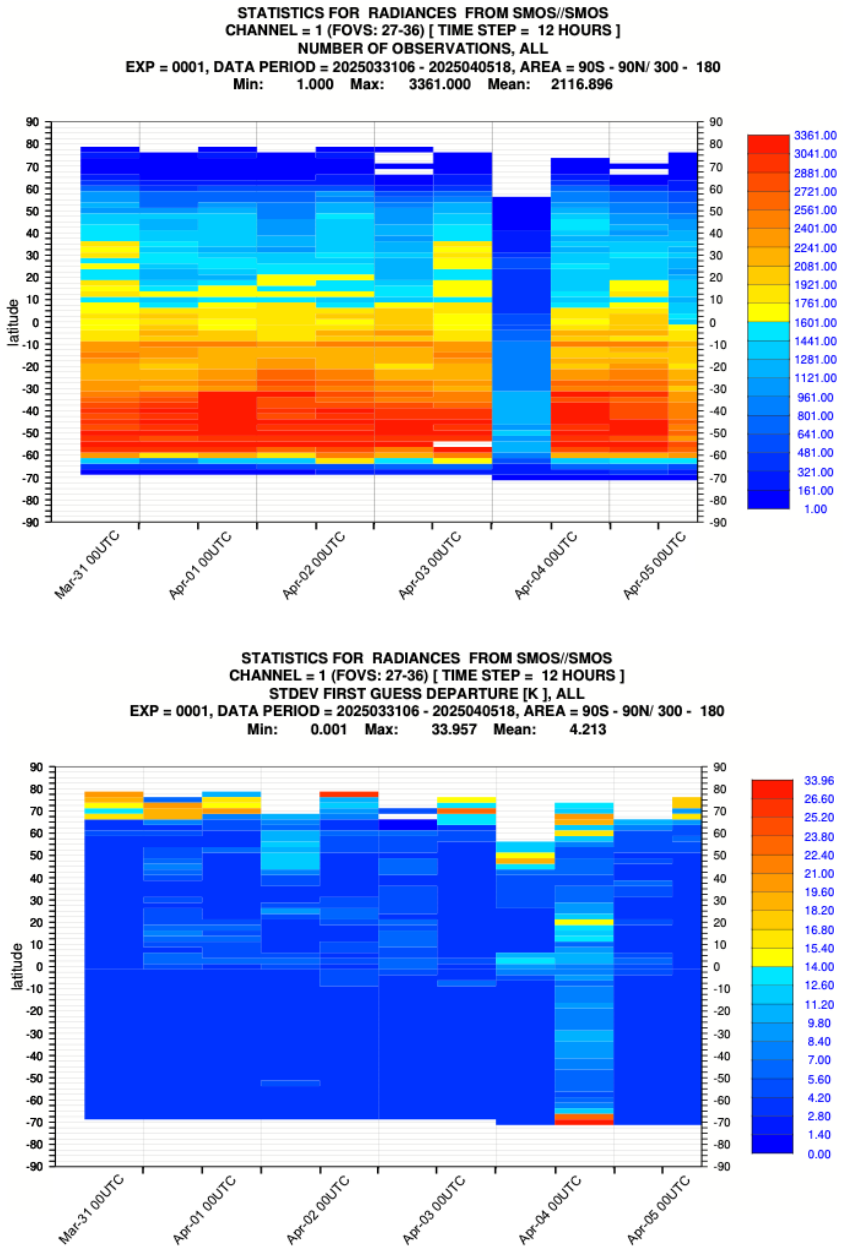

Figure 13. Hovmöller diagram of the number of observations (upper panel), and the standard deviation of the first guess departure (lower panel) over ocean for H polarisation and an incident angle 30° computed for 1-5 April 2025.

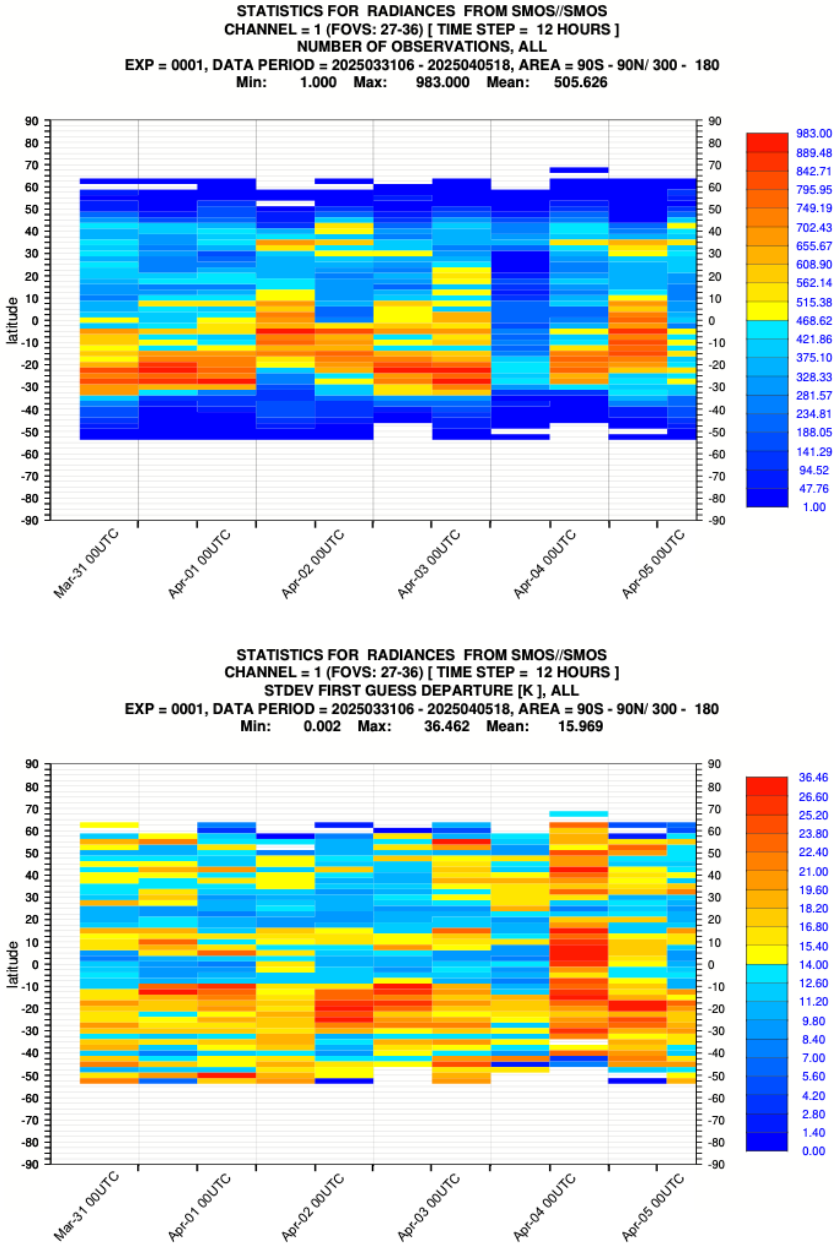

Figure 14. As Figure 13, but computed over land.

3.2. RFI anomaly over India and Sothern China November 2024 – January 2025

A map of the first-guess departure standard deviation over the performance period (Figure 8) revealed a prominent feature of extreme values over India and Southern China. Further investigation of monthly maps of the first-guess standard deviation for the performance period showed that this anomaly occurs from November 2024 through January 2025 (for example in November, shown in Figure 15), whereas outside of this timeframe, the affected areas were removed by the RFI filtering process (for example in October, shown in Figure 16). This suggests that a possible issue with the RFI filtering during November 2024 - January 2025. It is likely that the feature over India and China is in fact due to residual RFI contamination by a source over Myanmar that has been observed in previous

years. The observed negative first-guess departures may result from sidelobe effects inherent to the SMOS instrument design, even though the original RFI signal typically produces positive first-guess departures.

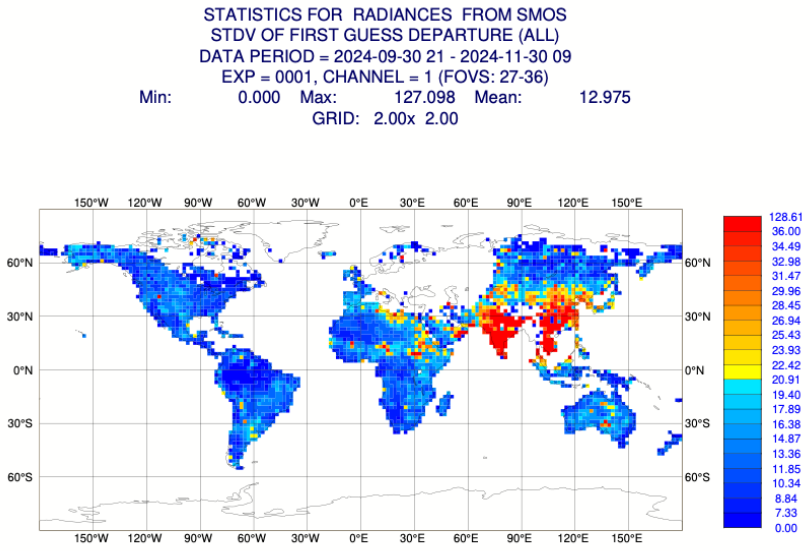

Figure 15: Gridded map plot showing the standard deviation of SMOS first-guess departures over land at 30° incidence angle, H polarisation covering in November 2024.

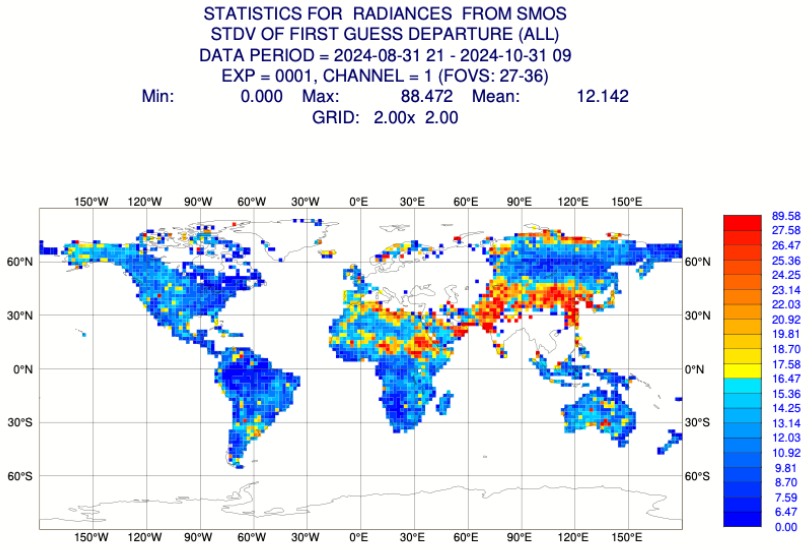

Figure 16: As in Figure 15, but for October 2024.

3.3. RFI anomaly over the Mediterranean in September 2024 – January 2025

Between September 2024 and January 2025, elevated first-guess standard deviations are observed in the Mediterranean as well as along the coasts of Southern Asia (Figure 17). This variability is likely

linked to RFI contamination, possibly from the sources over India and China reported in Section 3.2 as well as a possible source near the Mediterranean. The Mediterranean is removed in the RFI filtering from February 2025 onwards and the first-guess standard deviation near the South Asian coasts is reduced (Figure 18). During September and October 2024, the elevated variability in the Mediterranean and near South Asia coincides with increased first-guess standard deviations over the Arctic Ocean (Figure 17), contributing to the overall rise in oceanic first-guess standard deviation noted in the time series plots (Section 2.1, Figure 3). After October 2024, most of the Arctic Ocean is masked due to sea ice and the potential RFI effect over the Mediterranean and near the South Asian coasts becomes too small to significantly influence the time series, though it remains visible until November 2024 in the 15°–35°N band of the Hovmöller plot (Figure 6).

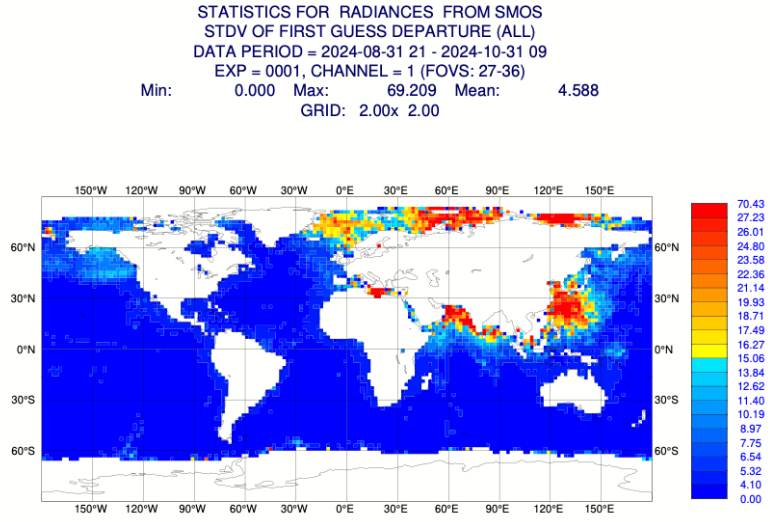

Figure 17: Gridded map plot showing the standard deviation of SMOS first-guess departures over ocean at 30° incidence angle, H polarisation covering for September - October 2024.

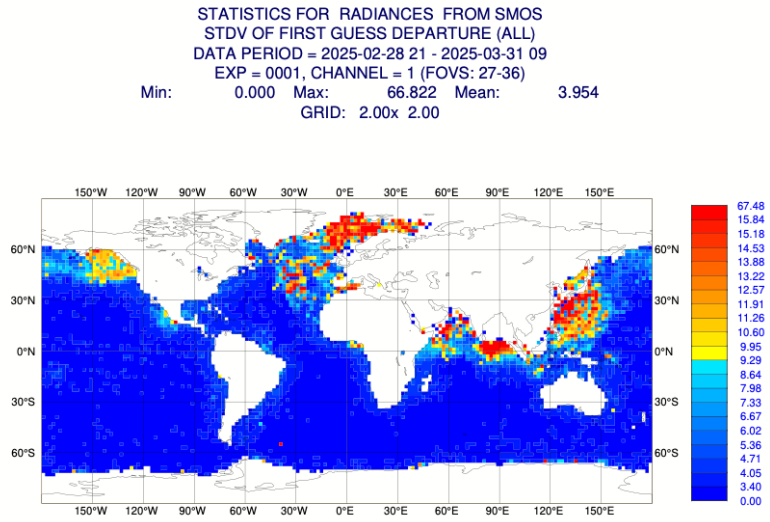

Figure 18: As Figure 17, but for March 2025.

3.4. Ocean anomaly November 2024 – February 2025

The Hovmöller plots presented in Section 2.2 (Figure 5) show an increase in the observation and first-guess departure standard deviations over ocean surfaces between 0 and 45°N from November 2024 to February 2025. This increase is most evident for an incidence angle of 20°, although its magnitude is significantly smaller than that observed during known RFI events. At the same time, the number of observations decreases over the Southern Hemisphere.

Similar anomalies occurred during the winters of 2021–22, 2022–23, and 2023–24 and are associated with solar activity. In short, strong solar activity can affect the accuracy of Faraday rotation due to increased uncertainty in the total electron content of the atmosphere. Within the ECMWF system, quality control applied to SMOS brightness temperatures excludes observations where the solar reflection flag is set; these observations are not included in the ODB files ingested by the model. The reduction in the number of observations seen in Figure 6 is thus a consequence of this quality screening. Although observations directly affected by solar reflection are removed, the solar signal spreads across the entire snapshot, leading to increased standard deviations in both observations and first-guess departures. A more detailed discussion of this effect is provided in Salonen et al. (2025).

3.5. Ocean signal contamination 20th March 2025

On 20th March, a sharp spike in the standard deviation of first-guess departures over the ocean was observed in the time series (Figure 3). Analysis of the Hovmöller diagrams for this period confirms increased standard deviations in both observations and first-guess departures between 35°N and 65°N on 20th March 2025 00UTC (Figure 19). This anomaly is followed by a notable reduction in observation counts over the same latitudes in the subsequent time step. An investigation of the spatial distribution of the first-guess departure standard deviations shows a large anomaly over the North Atlantic at 00UTC (Figure 20 top), and a gap in the observations near that region at 12UTC (Figure 20 bottom)

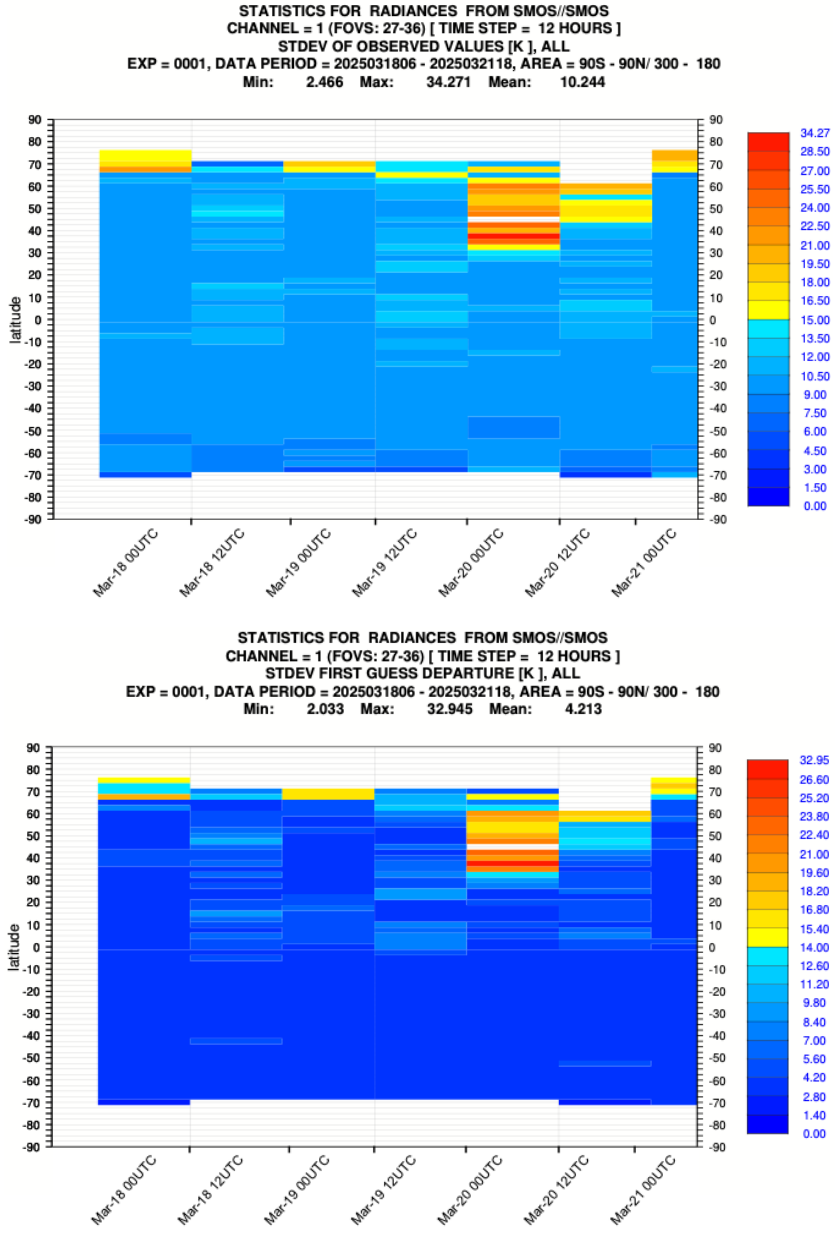

Figure 19. Hovmöller diagram of the observation standard deviation (top panel) and the first-guess departure standard deviation during 18 – 21 March for H polarisation and 30° incidence angle.

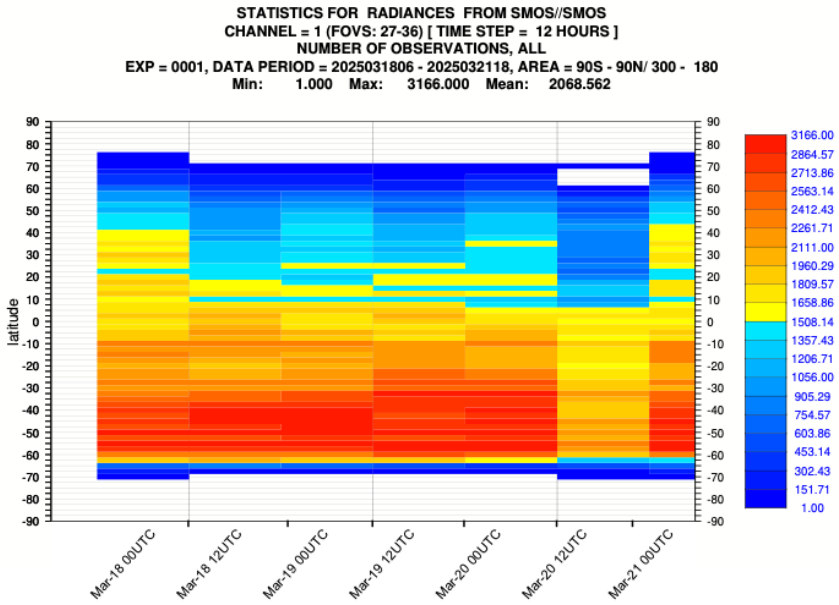

Figure 20. Hovmöller diagram of the number of observations between 18 – 21 March 2025 for H polarisation and 30° incidence angle.

An investigation by ESA colleagues revealed that the observed behaviour is caused by a short-lived RFI source over the Northeast Atlantic that leads to elevated observation standard deviations on 20th March 2025 and, consequently, higher first-guess deviations, and that is successfully removed through RFI control on 21st March 2025, leading to the lower observation counts then. Additionally, on 20th March, the SMOS MIRAS instrument also experienced a partition failure, which was resolved on 21st March, and which may have contributed to the anomalous behaviour that is observed.

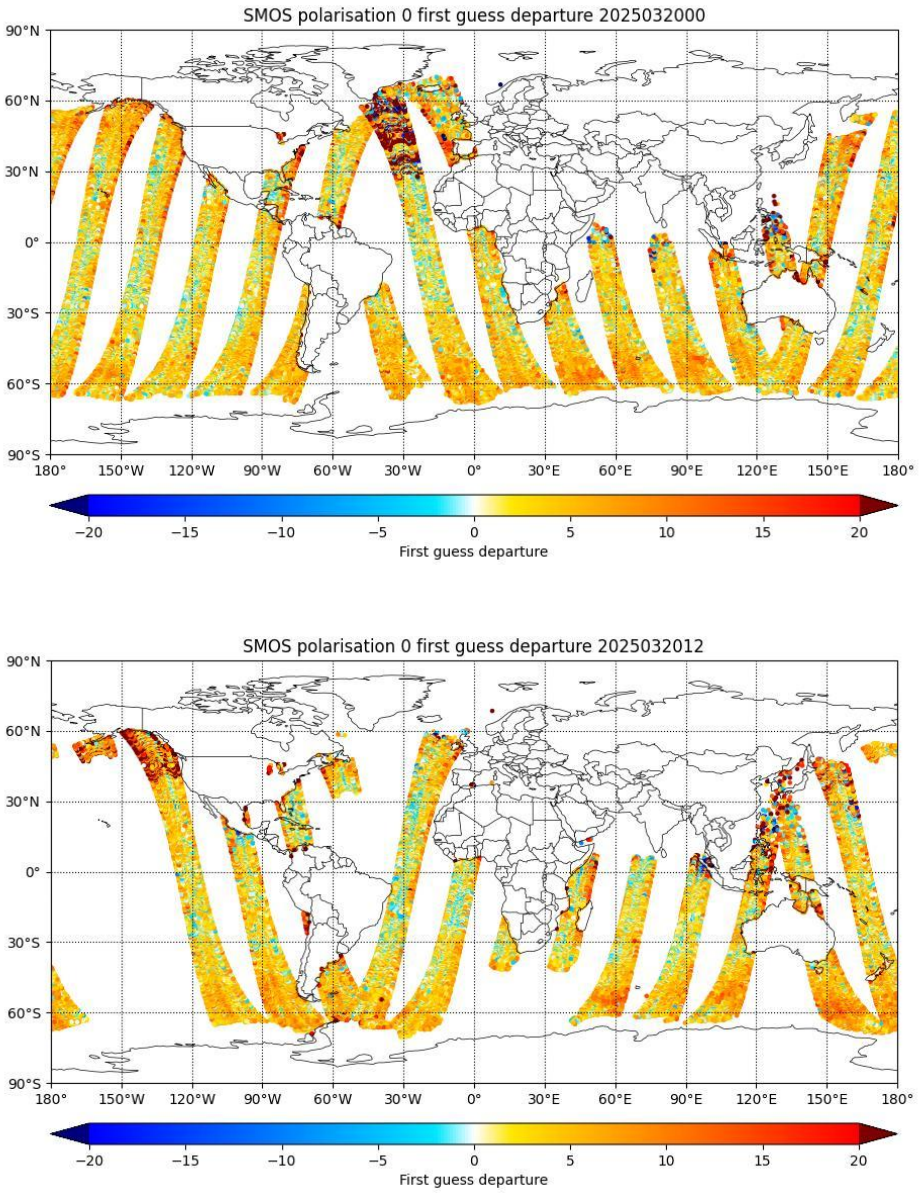

Figure 21. Map of the first guess departure over the ocean at 00UTC (top panel) and 12UTC (bottom panel) on 20th March 2025 at H polarisation.

3.6. Land signal contamination 5th March 2025

On 5th March, a sharp spike in the standard deviation of first-guess departures over land was observed (Figure 22 top), driven by an increase in the observation standard deviation (Figure 22 bottom). Unlike the event on 4th April, this anomaly was not preceded by or associated with a reduction in the number of observations. Instead, it appears to be a standalone increase in observation standard deviation between 15°N and 40°N around 00 UTC on 5th March. Examination of the spatial distribution of the statistics for this time step reveals a patch of elevated first-guess standard deviation over Northern Africa, with a secondary source over Mexico (Figure 23). Both patterns are associated

with a negative first guess and are possibly linked to short-lived sources of radio frequency interference (RFI) that were not properly filtered.

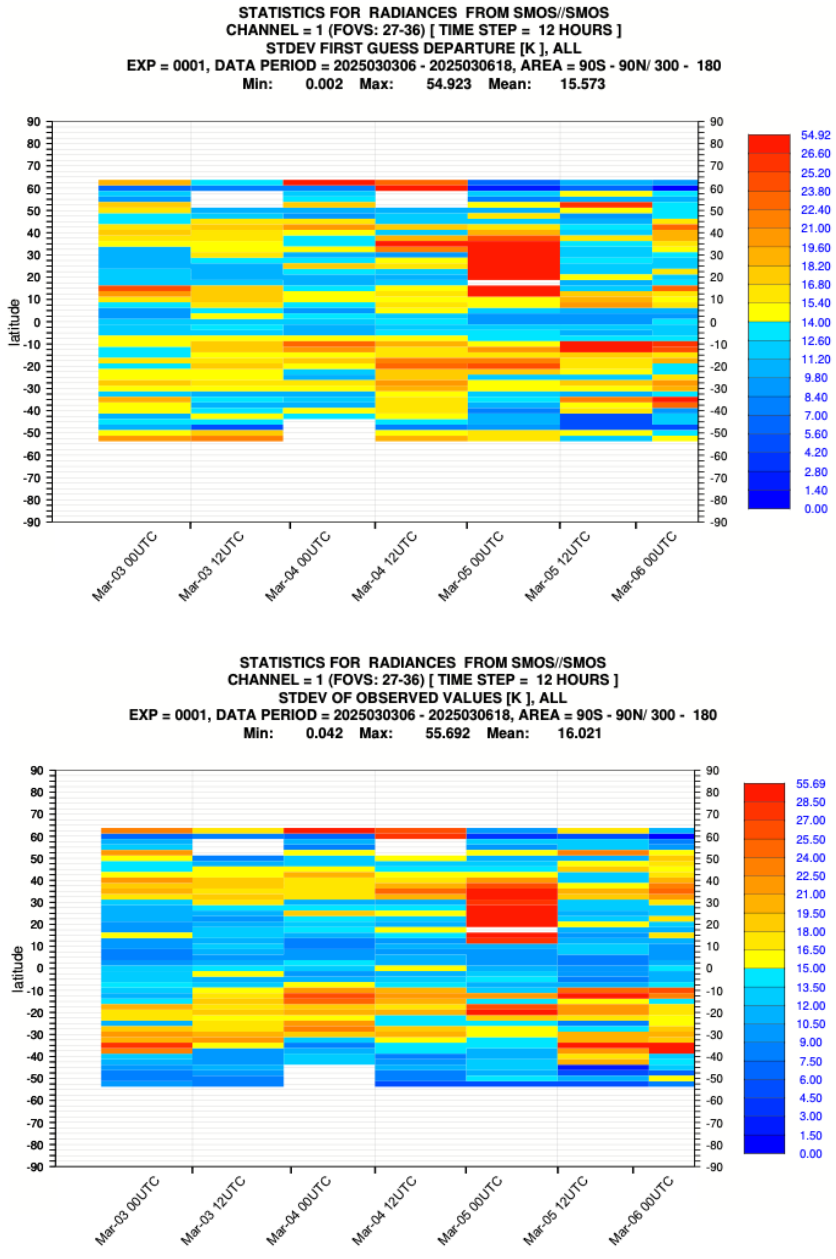

Figure 22. Hovmöller diagram of the first-guess standard deviation (top panel) and the observation standard deviation (bottom panel) over land between 3 – 6 March 2025 for H polarisation and 30° incidence angle.

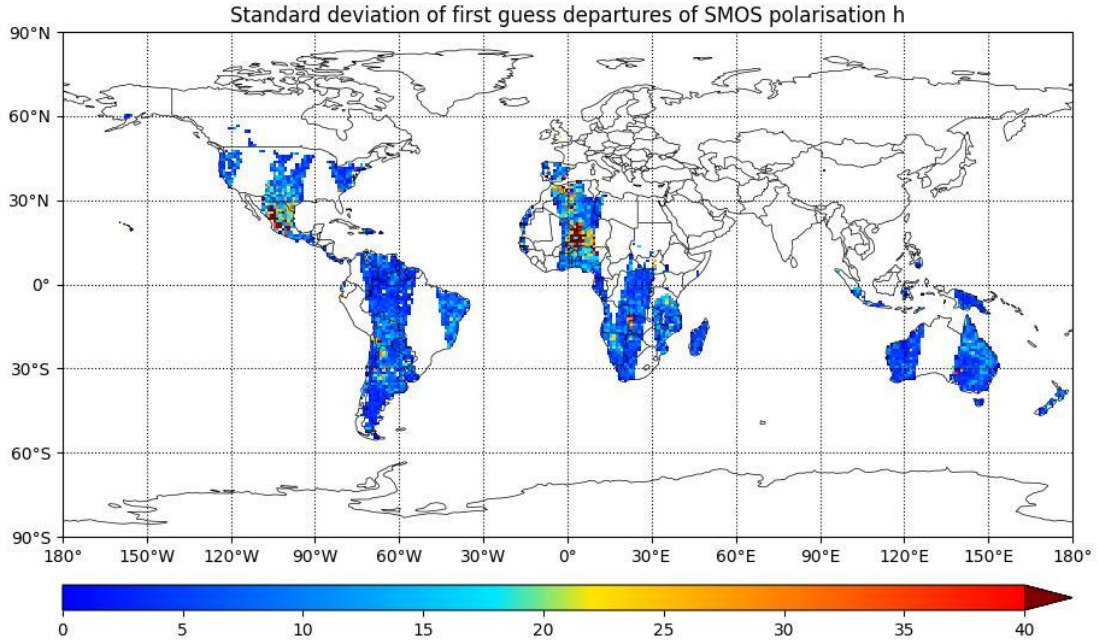

Figure 23. Map of the first-guess standard deviation at H polarisation at 00UTC on 5th March.

4. Analysis of Arm-A1 temperature increase impact

As part of the SMOS brightness temperature monitoring, we present an investigation into the potential impact of the Arm-A1 temperature increase on first-guess departures. During eclipse seasons, a rise in the temperature of Arm A Segment 1 onboard the SMOS satellite has been observed. This increase is likely due to age-related degradation of the thermo-optical properties of the Segment A1 radiators, which are most affected because of their increased sun exposure. Figure 24 shows that this temperature rise is particularly noticeable in early November and late January to early February. When the anomaly was first detected, Weston and de Rosnay (2020) assessed its possible influence on observed brightness temperatures (Tbs) and concluded that there was no clear evidence of an impact on SMOS first-guess departures in the ECMWF system. However, the Arm-A1 temperature has continued to increase each year (Figure 25), prompting a re-investigation to determine whether an effect can now be detected in the first-guess departures. For brevity, we will focus our analysis on an investigation of the November temperature peak.

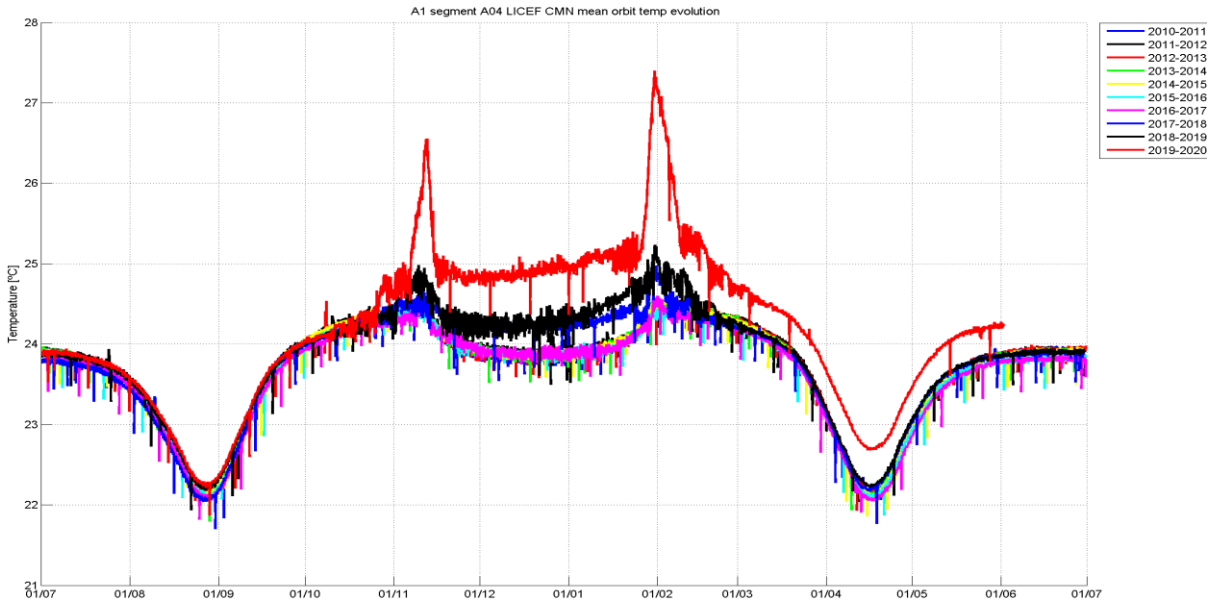

Figure 24. Time series of temperature of all units in Arm A Segment 1

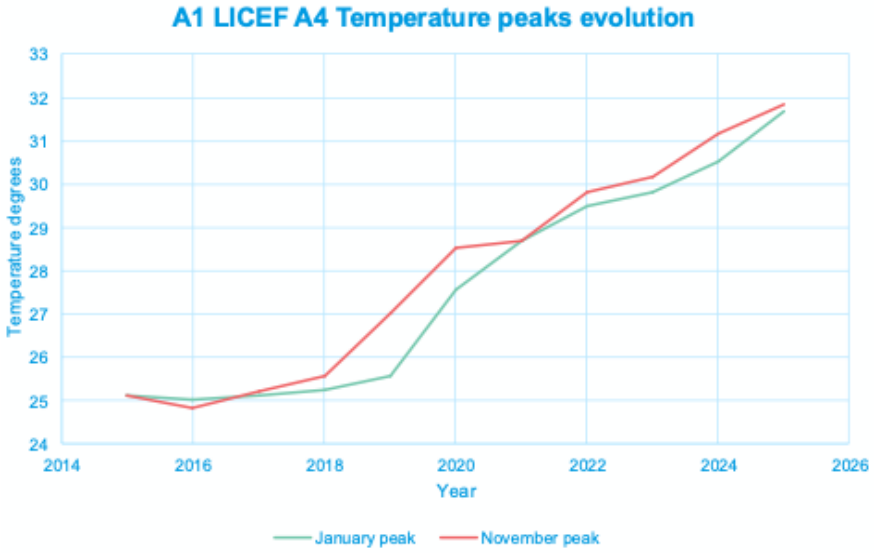

Figure 25. Arm-A Segment 1 temperature in January and November for 2015 – 2025 (from Jorge Fauste's presentation at the SMOS Quality Working Group meeting #41)

To assess whether the progressively increasing Arm-A1 temperature produces a detectable signal in the first-guess departures, we compare the global mean first-guess departures over the past four years (Figure 26). From 2021 to 2023, there is an apparent decrease in the global mean values over land. In 2024, the departures initially remain similar to 2023 but exhibit a sharp increase around 12th November when the IFS model changes from cycle 48r1 to 49r1, a transition which was accompanied by significant changes to the land climatological fields. However, attributing the 2021 – 2023 variations to the Arm-A1 temperature increase is challenging because the statistics are influenced by several other factors: (1) changes in the number of observations due to frozen soil filtering in the

Northern Hemisphere during boreal winter, (2) increasing RFI contamination leading to data removal, and (3) residual unfiltered RFI contamination affecting the signal, such as that reported over India and China between November 2024 and January 2025 (Section 3.2). To minimize these confounding effects, we restrict the analysis to the tropics, where data counts are relatively stable due to the absence of frozen soil. Additionally, we exclude regions around India, Myanmar, and China to reduce the influence of residual RFI. Figure 27 presents the November mean first-guess departures computed between 20°S and 10°N. The decrease observed in the global plots is not evident in the tropical time series, suggesting that the global trend was likely driven by variations in frozen soil extent and/or residual RFI contamination. The small year-to-year changes of the mean first-guess departures in the tropics correspond to similar variations seen in SMAP brightness temperatures for the same time period and geographical region (not shown). This consistent behaviour combined with the relatively stable behaviour in the tropics indicates that, despite rising Arm-A1 temperatures, no discernible impact on first-guess departure statistics can be detected at this stage.

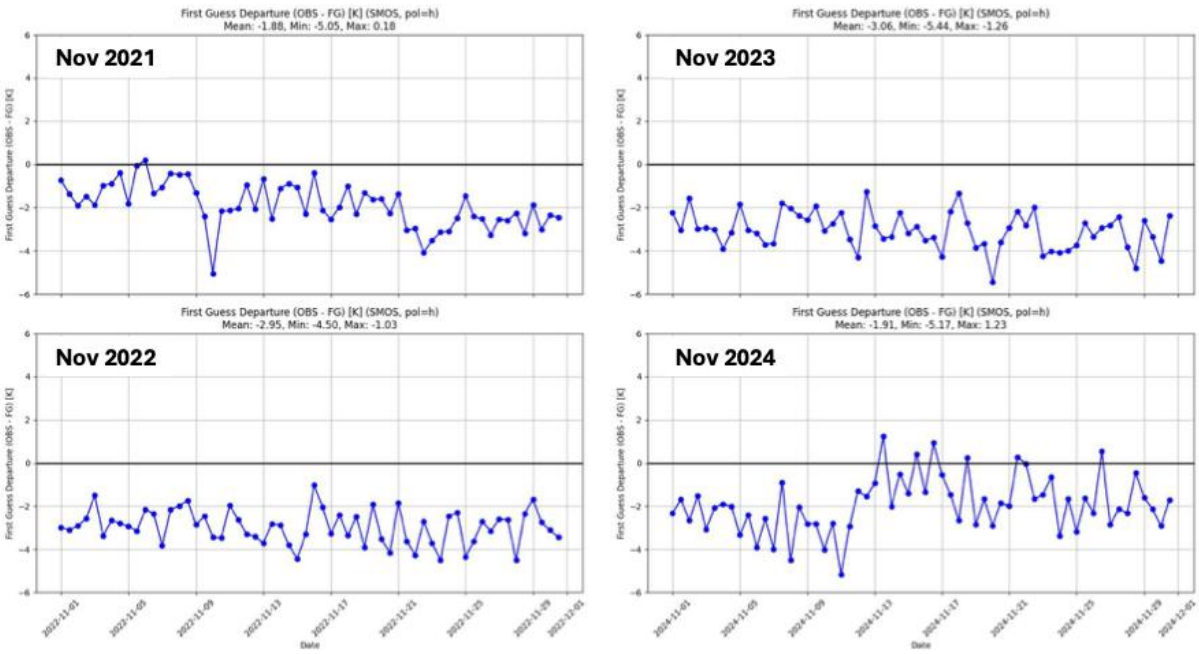

Figure 26. Time series of global mean first-guess departures for November 2021 – 2024 at 40° incidence angle and H-polarisation over land.

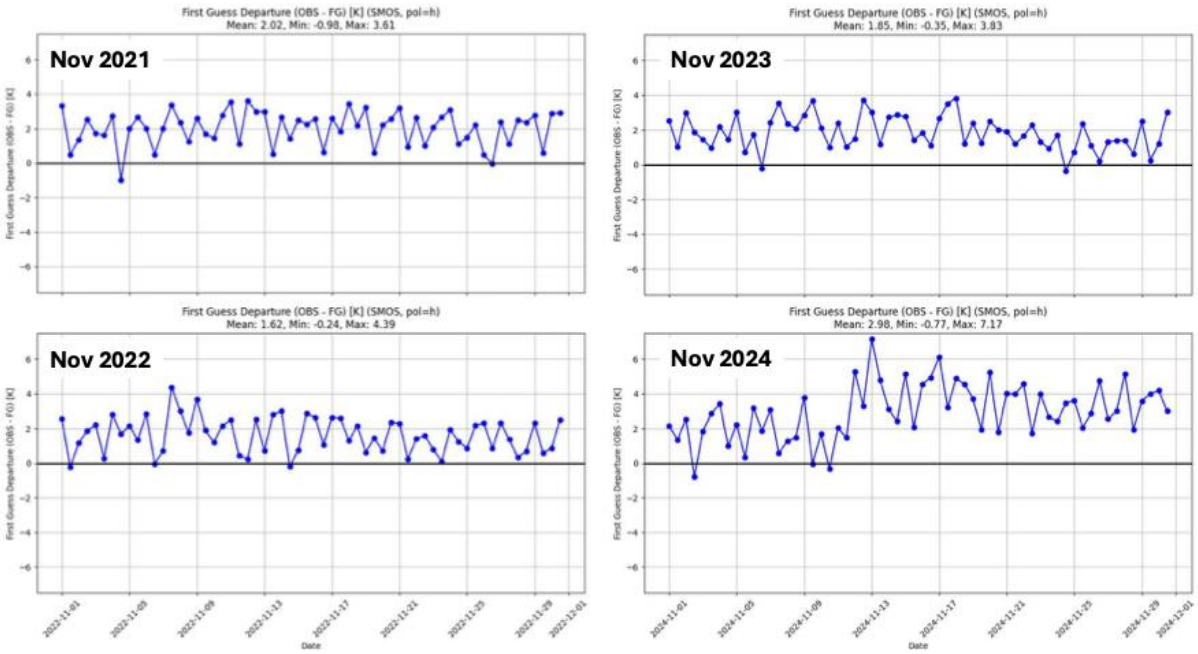

Figure 27. As in Figure 26, but computed for 20° S to 10° N only.

5. Comparisons to SMAP

Since 11th May 2021 the monitoring of the NASA Soil Moisture Active Passive (SMAP) instrument has also been part of the ECMWF operational system, using the same framework as the SMOS monitoring. SMAP was launched in 2015 and the instrument measures at L-band (1.41GHz) the same frequency as SMOS and therefore comparisons between the monitoring statistics for SMOS and SMAP are very relevant for unpicking observation and model issues in the first-guess departures.

The comparisons presented in Section 4.1 were made with data from September 2024 to August 2025 with the v724 SMOS L1 Tbs and most up-to-date SMAP Tbs in the operational system. The SMOS observations used in the comparison are limited to those with incidence angles between 39.5° and 40.5° which best match the 40° incidence angles of the SMAP observations. Also, the operational screening including the most up-to-date RFI screening is applied to the SMOS data. By contrast, SMAP has onboard RFI screening which is applied to the data before it arrives at ECMWF. CMEM with the same settings is used as the observation operator or both the SMOS and SMAP observations.

5.1. September 2024 to August 2025 comparison

Figure 28 shows that the standard deviation of first-guess departures is slightly smaller for SMAP than for SMOS for V polarization, while for H polarisation (not shown) the magnitudes are more similar. The SMAP mean first-guess departures exhibit a more negative bias, with a larger magnitude compared

to SMOS. Despite these minor differences, the overall statistics are largely comparable, consistent with previous findings reported by Weston and de Rosnay (2022), Salonen et al. (2024a), and Salonen et al. (2025). A brief SMAP data outage occurred in January 2025 due to a lapse in near-real-time product processing, which was caused by wildfires impacting Pasadena and JPL at that time.

Figure 29 shows that the gridded standard deviation values of first-guess departures are significantly smaller for SMAP than they are for SMOS with the largest differences in Asia and the middle East, both areas where there are significant RFI sources. This indicates that the onboard screening for SMAP is still doing a better job than the v724 SMOS screening. The differences shown in Figure 29 for 2024-2025 are larger than reported in Salonen et al. (2025) for 2023-2024, with the largest changes occurring over India and Southeast Asia, where they are likely caused by the potentially unfiltered RFI discussed in Section 3.2. In addition, over areas not affected by RFI, the SMAP standard deviation of first-guess departures are also smaller than for SMOS albeit to a slightly lesser degree. This indicates that SMAP has lower instrument noise than SMOS which is expected because the SMOS instrument was designed to reduce the noise by averaging over different incidence angles. In this analysis only a small range of SMOS incidence angles are used so there is no reduction in noise from the use of multiple incidence angles. Finally, compared to 2023-24, more areas are missing from this difference map, which is a direct consequence of the increased RFI and RFI filtering in 2024-25.

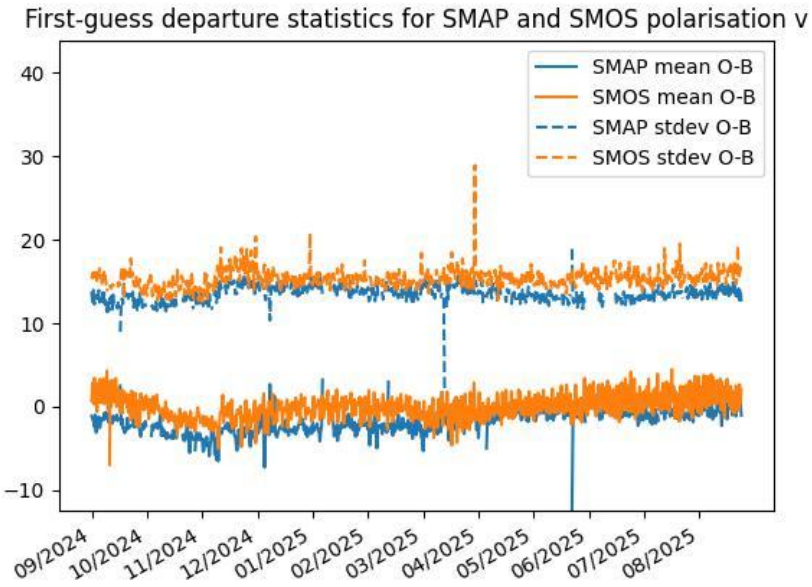

Figure 28: Time series of mean (solid lines) and standard deviation (dashed lines) of first-guess departures for SMAP (blue) and SMOS (orange) for V polarisation between 1st September, 2024 and 31st August, 2025.

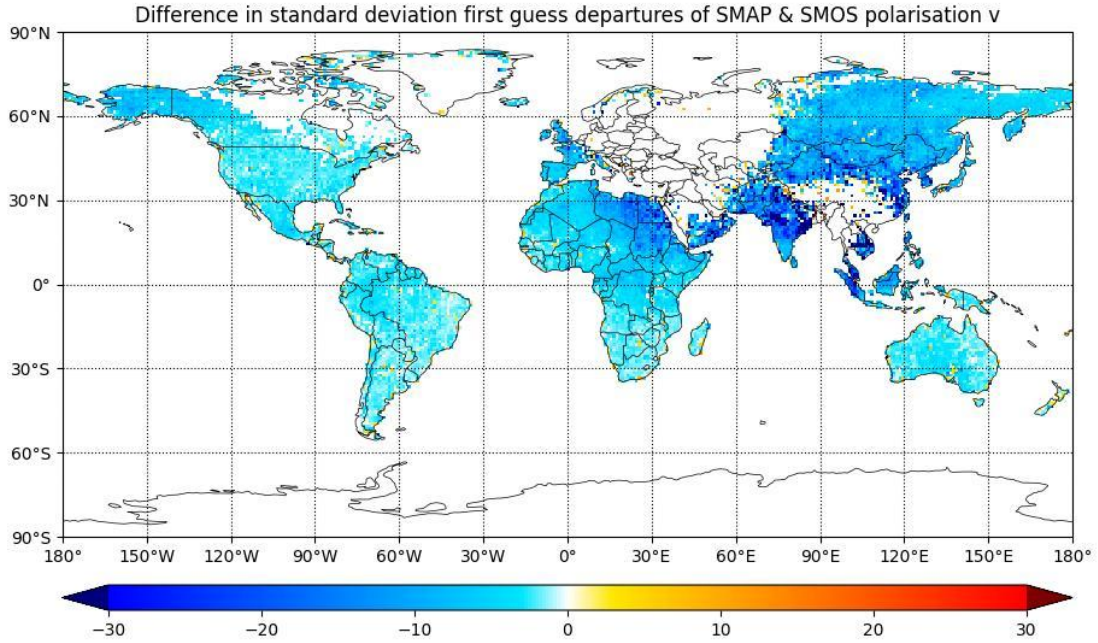

Figure 29: Difference in gridded standard deviation of first-guess departures for V polarisation between SMAP and SMOS. Statistics are calculated between 1st September, 2024 and 31st August, 2025

6. Future enhancements to the monitoring system

A potential area of interest for future development is a preliminary investigation into the feasibility of a machine learning (ML)-based observation operator. Such an investigation is motivated by several factors, including the growing desire to transition from retrieval assimilation toward radiance data assimilation at ECMWF. An ML-based observation operator could also help address outstanding questions, such as whether the observed performance differences between H and V polarisation (Section 2.1) are driven by instrument characteristics or by limitations in the currently used physically based CMEM observation operator for the two polarisations. Furthermore, ML approaches may enable a more sophisticated representation of surface properties, particularly the influence of surface winds on brightness temperatures over the ocean.

In addition, developments in the ECMWF land surface model are ongoing to investigate the potential of a finer vertical discretization in the soil. This development is highly relevant to better represent the top-layers soil moisture dynamics, with expected potential improvements in model forward modelling capabilities.

References

de Rosnay, P., J. Muñoz-Sabater, C. Albergel, L. Isaksen, S. English, M. Drusch, J.-P. Wigneron: SMOS brightness temperature forward modelling and long term monitoring at ECMWF. Remote Sens. Environ., 237 (2020): 111424. https://doi.org/10.1016/j.rse.2019.111424

Salonen K., P. Weston, P. de Rosnay: "Annual SMOS brightness temperature monitoring report", ESA SMOS ESL contract 4000130567/20/I-BG, February 2024a doi:10.21957/64e9d1fcec, 2024a98

Salonen, K., Weston, P., and de Rosnay, P.: Quality control plan for brightness temperature monitoring – 2024b. ESA contract report. SMOS ESL contract 4000130567/20/I-BG, 2024b

Salonen K., P. Weston, P. de Rosnay: "Annual SMOS brightness temperature monitoring report", ESA SMOS ESL contract 4000130567/20/I-BG, January 2025 doi: 10.21957/8f6b3808fa, 2025

Saunders, R., Hocking, J., Turner, E., Rayer, P., Rundle, D., Brunel, P., Vidot, J., Roquet, P., Matricardi, M., Geer, A., Bormann, N., and Lupu, C.: An update on the RTTOV fast radiative transfer model (currently at version 12), Geosci. Model Dev., 11, 2717–2737, https://doi.org/10.5194/gmd-11-2717-2018, 2018.

Weston, P., P. de Rosnay: Annual SMOS brightness temperature monitoring report - 2021/22. ESA contract report. SMOS ESL contract 4000130567/20/I-BG, December 2022b

Weston and de Rosnay; SMOS brightness temperature monitoring quality control review and enhancements, *13*(20), 4081, Remote Sensing, 2021 https://doi.org/10.3390/rs13204081

Weston and de Rosnay; Effects of the SMOS Arm A1 temperature increase on first-guess departures, ESA SMOS ESL contract 4000130567/20/I-BG, November 2020

Weston P., K. Salonen, P. de Rosnay: "Quarter 2 2025: Operations Service Report", ESA SMOS ESL contract 4000130567/20/I-BG, July 2025